



Cite this: RSC Adv., 2017, 7, 8295

## Cd<sub>2</sub>SnO<sub>4</sub> transparent conductive oxide: a promising alternative candidate for highly efficient hybrid halide perovskite solar cells†

Dong Liu,‡ Shengqiang Ren,‡ Xiao Ma, Cai Liu, Lili Wu,\* Wei Li, Jingquan Zhang,\* and Lianghuan Feng

Organic–inorganic hybrid perovskite solar cells have attracted significant research attention in terms of perovskite materials, fabrication, device architecture, and interfacial engineering to increase their power conversion efficiency (PCE). However, the state-of-the-art front electrode of perovskite solar cells is mainly focused on indium tin oxide (ITO) and fluorine-doped tin oxide (FTO). To further improve the optical characteristics of front electrodes for perovskite devices, it is necessary to explore a new and suitable transparent conductive oxide material. Herein, we introduce a Cd<sub>2</sub>SnO<sub>4</sub> film for constructing a perovskite device with a novel structure. The as-prepared Cd<sub>2</sub>SnO<sub>4</sub> film shows higher optical transmission in the visible region compared to the FTO substrate. The matching energy band alignment can ensure efficient carrier transport and collection between the TiO<sub>2</sub> layer and Cd<sub>2</sub>SnO<sub>4</sub> electrode. The higher PCEs with an average of 15.58% under AM 1.5 irradiation for Cd<sub>2</sub>SnO<sub>4</sub>-based perovskite solar cells were obtained compared to those of the FTO-based devices. This renders the Cd<sub>2</sub>SnO<sub>4</sub> film a promising transparent conductive oxide candidate for highly efficient perovskite solar cells. However, the toxicity of lead and cadmium components still remain a major concern for its commercial applications.

Received 22nd November 2016  
 Accepted 26th December 2016

DOI: 10.1039/c6ra27146d  
[www.rsc.org/advances](http://www.rsc.org/advances)

## Introduction

In recent years, organic/inorganic perovskite hybrid photovoltaic devices have attracted considerable attention due to the abnormally excellent optical and electrical properties, such as ambipolar charge transport, high absorption coefficient, and wide band gap tunability, of perovskite materials.<sup>1–4</sup> The power conversion efficiency has dramatically increased over the last few years. A PCE of up to 20% was obtained based on a p-i-n device architecture consisting of FTO/TiO<sub>2</sub>/perovskite/HTM/Au *via* vacuum flash-assisted solution process.<sup>5</sup> Note that these large-area perovskite devices show great potential for commercial application. For the p-i-n device architecture fabrication, the conventional devices have multiple layers including a front electrode, electron transport layer, perovskite layer, hole transport material (HTM) layer, and metal back electrode. Inverted planar heterojunction perovskite solar cells employ indium-doped-tin oxide, hole transport layer, perovskite layer,

electron transport layer, and metal back electrode. The main research studies for investigating the performance of perovskite solar cells have been carried out on the interfacial modification,<sup>6,7</sup> perovskite materials,<sup>8–10</sup> stability,<sup>11</sup> *etc.* Improving the optical characteristics of the front electrode plays an important role in perovskite solar cells. However, the current sputtered transparent conductive oxides for perovskite solar cells are based on tin-doped indium-oxide and fluorine-doped tin oxide. It is necessary to find excellent transparent conductive oxide materials to realize high performance perovskite solar cells. Recently, other novel transparent conductive materials were employed as electrode layers to fabricate the perovskite-based hybrid solar cells, as shown in Table 1. The oxidized Ni/Au electrode was developed for perovskite solar cells with a conventional architecture, which exhibited potential applications for cost-effective, low weight, and stable solar cells.<sup>12</sup> Copper nanowires as a vacuum-free and noble-metal-free transparent top electrode in perovskite solar cells were utilized and they exhibited promising device performance.<sup>13</sup> Conducting polymers have been used as transparent electrodes to realize high efficiency, good flexibility, and low-cost perovskite planar heterojunction solar cells on flexible substrates.<sup>14–16</sup> Highly transparent graphene, replacing the conventional transparent conductive oxide, had been applied in highly efficient perovskite solar cells.<sup>17</sup>

In addition, for conventional transparent conductive oxides used for commercial applications, the sheet resistance and

Institute of Solar Energy Materials and Devices, College of Materials Science and Engineering, Sichuan University, Chengdu, 610064, China. E-mail: [wulily77@163.com](mailto:wulily77@163.com); [zhangjq@scu.edu.cn](mailto:zhangjq@scu.edu.cn); Fax: +86 28 85412542; Tel: +86 28 85412542

† Electronic supplementary information (ESI) available: Detailed energy band parameters of the TiO<sub>2</sub> and Cd<sub>2</sub>SnO<sub>4</sub> films; AFM images for FTO and Cd<sub>2</sub>SnO<sub>4</sub> layers; histograms of their devices efficiency; stability of FTO-based device stored in relative humidity of ~10% for 27 days. See DOI: [10.1039/c6ra27146d](https://doi.org/10.1039/c6ra27146d)

‡ These authors contributed equally to this work.



Table 1 Reported transparent conductive materials in the references

TCO	Device architecture	References
Au:NiO <sub>x</sub>	Au:NiO <sub>x</sub> /perovskite/C <sub>60</sub> /BCP/Al	12
PH1000	PH1000/Pedot:PSS/perovskite/PCBM/Al	14–16
Graphene	Graphene/MoO <sub>x</sub> /Pedot:PSS/perovskite/C <sub>60</sub> /BCP/LiF/Al	17
Nanowires	FTO/TiO <sub>2</sub> /perovskite/HTM/nanowires	13

transmittance spectra of FTO do not show significant changes before and after thermal heating at 500 °C. Note that the electrical properties of ITO show significant changes as compared to those of FTO. This indicates that FTO shows relatively high stability against thermal heating. Therefore, ITO as a TCO layer for TiO<sub>2</sub> structure devices is unsuitable. Moreover, SnO<sub>2</sub> films prepared by sputtering show an average transmission of about 80% with a sheet resistivity of 10 Ω per square. Moreover, they possess a narrow range of adjustability and flexibility for their optoelectrical properties and manufacturing costs. Optimizing the device performance or processing cost adhesion not only improves their properties, but also provides greater latitude in the material treatment process. Considering the photovoltaic performance and manufacturing cost of the perovskite solar cell modules, conventional transparent conductive oxides have shown a lower design latitude.

Cadmium stannate (Cd<sub>2</sub>SnO<sub>4</sub>) is a well-known transparent conductive oxide (TCO) that has been used in CdTe solar cells owing to its high electrical conductivity and optical transmission in the visible range compared to those of FTO.<sup>18–20</sup> The thin film has demonstrated an electron mobility and resistivity of up to 100 cm<sup>2</sup> V<sup>-1</sup> s<sup>-1</sup> and 1.28 × 10<sup>-4</sup> Ω cm, respectively.<sup>19,21</sup> It is a n-type semiconductor material with a band gap of around 3.0 eV, in which oxygen vacancies act as donor states.<sup>21</sup> The conduction band edge position is closely matched with the conduction band minimum of TiO<sub>2</sub>. The structure and optical characteristics of cadmium stannate thin films can be further tailored by gamma irradiation<sup>21</sup> and suitable dopants, such as In and Sb.<sup>22</sup> Furthermore, Cd<sub>2</sub>SnO<sub>4</sub> thin films require cost-effective preparation techniques including radio frequency magnetron sputtering,<sup>23</sup> sol-gel,<sup>24</sup> dip coating,<sup>25</sup> and spray pyrolysis.<sup>22</sup> In addition to acquiring both high conductivity and stretch ability of the electrodes, Cd<sub>2</sub>SnO<sub>4</sub> transparent conductive oxide renders these as excellent candidates for realizing high performance solar cells. However, serious issues of these materials cannot be ignored. Tin and cadmium are rare elements. Moreover, lead and cadmium components can cause serious environmental pollution. The material cost and toxicity should be considered for their application and commercialization in the future. Reducing the cost of the preparation process and reasonable device encapsulation should be carefully considered for rectifying these problems.

Herein, we exploited the Cd<sub>2</sub>SnO<sub>4</sub> film to serve as a transparent conductive oxide for the Cd<sub>2</sub>SnO<sub>4</sub>/bl-TiO<sub>2</sub>/mp-TiO<sub>2</sub>/perovskite/spiro-MeOTAD/Au device. The presence of a Cd<sub>2</sub>SnO<sub>4</sub> layer exhibited superior transmittance in the visible and NIR regions compared to the FTO substrate. Energy band diagram

and interfacial features were discussed by constructing the thermal equilibrium energy band structure diagram from the vacuum energy level. Higher PCEs with an average of 15.58% under AM 1.5 irradiation for Cd<sub>2</sub>SnO<sub>4</sub>-based perovskite solar cells were obtained compared to those of the FTO-based devices. We believe that Cd<sub>2</sub>SnO<sub>4</sub> film will be the most promising candidate for high performance perovskite solar cell applications.

## Experimental

### Materials

Lead iodide, lead chloride, titanium diisopropoxide bis(acetylacetone) (75% in isopropanol), and *N,N*-dimethylformamide were purchased from Alfa Aesar. Chlorobenzene was purchased from Acros. Spiro-MeOTAD was purchased from Lumtec. CH<sub>3</sub>NH<sub>3</sub>I was prepared using the method reported in literature.<sup>26</sup> The conventional transparent conductive oxide substrate was FTO (Pilkington, thickness: 3.2 mm, sheet resistance 10 Ω per square). Cd<sub>2</sub>SnO<sub>4</sub> thin films used as solar cell substrates were deposited by radio frequency magnetron sputtering on corning glass (sheet resistance: ~10 Ω per square).

### Device fabrication

The devices Cd<sub>2</sub>SnO<sub>4</sub> (and FTO)/bl-TiO<sub>2</sub>/mp-TiO<sub>2</sub>/CH<sub>3</sub>NH<sub>3</sub>-PbI<sub>3-x</sub>Cl<sub>x</sub>/spiro-OMeTAD/Au were fabricated. First, the transparent conductive oxide substrates were cleaned with a detergent. They were then sonicated with high purity water in an ultrasonic bath for 15 min, and finally placed in boiling water for 5 min, and the abovementioned steps were repeated three times. TiO<sub>2</sub> blocking layer (bl-TiO<sub>2</sub>) of 40 nm was prepared by spray pyrolysis using titanium diisopropoxide bis(acetylacetone) (75% in isopropanol) (diluted in ethanol in a volumetric ratio of 1 : 40) at 450 °C. To prepare a 120 nm mesoporous TiO<sub>2</sub> layer (mp-TiO<sub>2</sub>), diluted 18NR-T (Dyesol 18NR-T : ethanol = 2 : 15, m/m) was spin coated on the substrate at 4200 rpm for 40 s, and then annealed at 500 °C for 60 min. CH<sub>3</sub>NH<sub>3</sub>I was mixed with PbI<sub>2</sub> and PbCl<sub>2</sub> (mole ratio of PbI<sub>2</sub> : PbCl<sub>2</sub> : CH<sub>3</sub>NH<sub>3</sub>I = 1 : 1 : 4, 50 wt%) in DMF. Stirring at 65 °C and filtration led to transparent precursor solution. To obtain CH<sub>3</sub>NH<sub>3</sub>PbI<sub>3-x</sub>Cl<sub>x</sub> films, the precursor solution was spin-coated on the mp-TiO<sub>2</sub> layer at 4000 rpm for 50 s, and then placed in a drying cabinet for 50 min (at 20% relative humidity), followed by thermal annealing at 100 °C for 75 min. The spiro-MeOTAD layer was spin coated on the perovskite layer at 2000 rpm for 30 s from a hybrid solution (dissolved in chlorobenzene, 72 mg/1 mL; 17 μL Li-bis(trifluoromethanesulfonyl)-imide (Li-TFSI), dissolved in acetonitrile, 520 mg mL<sup>-1</sup> and 20 μL *tert*-butylpyridine (*t*-BP)). The gold film of 100 nm was deposited on the spiro-MeOTAD layer as the back electrode by thermal evaporation technology.

### Characterization

The transmittance spectra were obtained using a Perkin Elmer Lambda 950 Spectrometer. The ultraviolet photoelectron spectroscopy (UPS) measurements of Cd<sub>2</sub>SnO<sub>4</sub> film were performed using Thermo Scientific Escalab 250Xi. The SEM images were



obtained using a Hitachi S-5200. Atomic force microscopy (AFM) measurements of the samples were conducted using Bruker multimode 8 scanning probe microscopy. The photo  $I$ - $V$  curves were obtained using a Keithley 2400 Source meter under simulated AM 1.5G sunlight irradiation (100 mW cm $^{-2}$ ) (ABET technologies Sun 2000 solar simulator). The light intensity was calibrated using a GaAs reference cell certificated by NREL. The dark  $I$ - $V$  curves were obtained using an Agilent 4284A precision LCR meter. The external quantum efficiency (EQE) was measured using a QEX10 measurement system (PV Measurements, Inc.). The active area of the devices was typically 0.15 cm $^2$ . The steady-state and time-resolved photoluminescence spectra were obtained using a FLS 980 fluorescence spectrometer (Edinburgh Instruments) with excitation at 655 nm.

## Results and discussion

The transmittance spectra of the FTO and Cd<sub>2</sub>SnO<sub>4</sub> transparent conductive oxide substrates with a similar sheet resistivity of 10  $\Omega$  per square are illustrated in Fig. 1(a). Typically, to obtain a similar sheet resistivity with FTO, the thickness of the Cd<sub>2</sub>SnO<sub>4</sub> film was controlled to  $\sim$ 250 nm during the sputter deposition process. As shown in Fig. 1(a), the Cd<sub>2</sub>SnO<sub>4</sub> film showed better optical transmittance than the SnO<sub>2</sub>:F film in the vis-NIR region. The onset of the transmittance spectra showed a slight difference due to difference in the optical band gap ( $E_g$ ). According to the Tauc equation,<sup>27</sup>

$$\alpha h\nu = A(h\nu - E_g)^n \quad (1)$$

where  $\alpha$ ,  $A$ , and  $h$  represent the absorption coefficient, constant, and Planck constant, respectively. For a direct band gap semiconductor,  $n = 0.5$ , the optical band gap of Cd<sub>2</sub>SnO<sub>4</sub> film can be calculated from eqn (1), as shown in Fig. 1(b). As is known, the optical band gap of a SnO<sub>2</sub>:F film is 3.7 eV,<sup>28</sup> which is higher than that of a Cd<sub>2</sub>SnO<sub>4</sub> film ( $\sim$ 3.05 eV), leading to a slight red shift for the Cd<sub>2</sub>SnO<sub>4</sub> film compared to the FTO substrate. It was observed that the transmittance in the 400–900 nm region of the Cd<sub>2</sub>SnO<sub>4</sub> film was much better than that of the SnO<sub>2</sub>:F film under similar sheet resistivity conditions. This suggests that thinner films will be required to obtain the same excellent optical properties (the thickness of  $\sim$ 400 nm for FTO). In addition, the transmittance of a Cd<sub>2</sub>SnO<sub>4</sub> film at 1000 nm can still be up to  $\sim$ 86% compared to that of FTO (<80%). This also

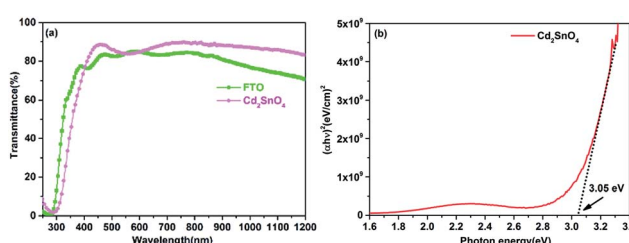


Fig. 1 (a) Transmittance spectra of different transparent conductive oxide substrates with similar sheet resistivity of 10  $\Omega$  per square and (b) plot of  $(\alpha h\nu)^2$  versus photon energy ( $h\nu$ ) for Cd<sub>2</sub>SnO<sub>4</sub> film.

shows higher transmittance in the near-infrared region, which is of great benefit for the applications of perovskite-based tandem devices, such as monolithic perovskite/silicon tandem solar cells.<sup>29–31</sup>

The UPS spectrum was obtained to calculate the work function of the Cd<sub>2</sub>SnO<sub>4</sub> layer, as shown in Fig. 2. According to the linear fit at the secondary electron onset, we can obtain the sample inelastic cut-off ( $E_{\text{Cutoff}}$ ) of 17.02 eV. In the valence band emission region, the distance between the valence band ( $E_{\text{VBM}}$ ) and Fermi edge ( $E_{\text{Fermi}}$ ) can be estimated to 3.03 eV from the intercept of the linear fitting plot. Based on the Einstein's photoemission law, the work function ( $\Phi$ ) can be described as follows:<sup>32</sup>

$$\Phi = h\nu - (E_{\text{Cutoff}} - E_{\text{Fermi}}) \quad (2)$$

where  $h\nu$  represents the photon energy. The work function of the Cd<sub>2</sub>SnO<sub>4</sub> film was calculated to be 4.2 eV. Based on the optical band gap from the transmittance spectra, the electron affinity ( $\chi$ ) can be written as

$$\chi = \Phi + E_{\text{VBM}} - E_g \quad (3)$$

According to eqn (3), we can obtain an  $\chi$  value of 4.18 eV for the Cd<sub>2</sub>SnO<sub>4</sub> film. This electron affinity for Cd<sub>2</sub>SnO<sub>4</sub> film is comparable to that of FTO (4.4 eV (ref. 28)) transparent conductive oxide film. This indicates that the Cd<sub>2</sub>SnO<sub>4</sub> film shows a compatible energy level for a transparent conductive oxide substrate.

To investigate the effect of energy band matching at the Cd<sub>2</sub>SnO<sub>4</sub>/TiO<sub>2</sub> interface, the thermal equilibrium energy band diagram of the Cd<sub>2</sub>SnO<sub>4</sub>/TiO<sub>2</sub> interface is shown in Fig. 3. Typically, the energy band parameters of TiO<sub>2</sub> are reported in another study.<sup>33</sup> The energy band parameters of the TiO<sub>2</sub> and Cd<sub>2</sub>SnO<sub>4</sub> layers are listed in ESI Table S1.† In the front contact region of the photovoltaic devices, the electron-transporting layer/transparent conductive oxide layer interface has a key influence on electron collection. The high resistivity of the TiO<sub>2</sub> layer coated on the Cd<sub>2</sub>SnO<sub>4</sub> layer provides reasonable electronic levels with favorable electron collection, associating with low recombination at the TiO<sub>2</sub>/electrode interface.<sup>34</sup> As shown in Fig. 3, the work function of the TiO<sub>2</sub> layer is higher than that of Cd<sub>2</sub>SnO<sub>4</sub> at the Cd<sub>2</sub>SnO<sub>4</sub>/TiO<sub>2</sub> interface, which renders it

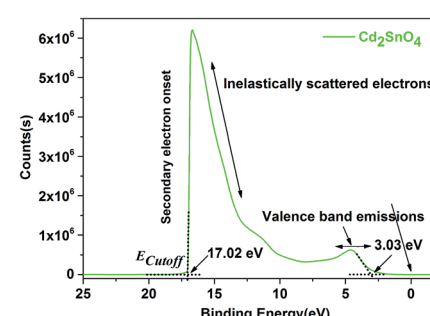


Fig. 2 UPS spectrum of Cd<sub>2</sub>SnO<sub>4</sub> film on glass.



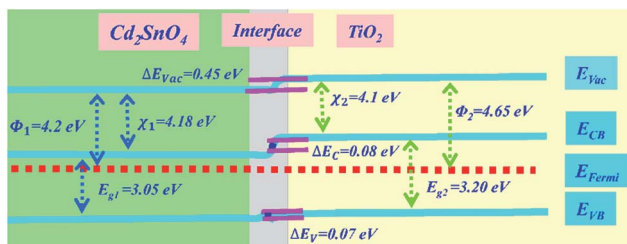


Fig. 3 Energy band structure diagram of the  $\text{TiO}_2/\text{Cd}_2\text{SnO}_4$  layer interface.

possible for charge injection and collection from  $\text{TiO}_2$  to the electrode. The energy band bending of 0.45 eV occurs in this heterojunction. The very small band barrier  $\Delta E_c$  of 0.08 eV exists at the interface, enhancing the interfacial charge transport and decreasing the electronic reflux and charge accumulation.<sup>35</sup> It is reasonable to form an energy band structure-matching between the  $\text{Cd}_2\text{SnO}_4$  electrode and electron-transporting layer for an efficient charge transport process. This suggests that the  $\text{Cd}_2\text{SnO}_4$  layer is a promising and excellent transparent conductive oxide substrate for  $\text{TiO}_2$ -based perovskite solar cells.

To investigate the effect of interfacial recombination on the  $\text{Cd}_2\text{SnO}_4$  and  $\text{TiO}_2$  layers,  $\text{Cd}_2\text{SnO}_4$  (and FTO)/bl- $\text{TiO}_2$ /spiro-OMeTAD/Au devices were prepared. Fig. 4(a–e) shows SEM and AFM images of the bl- $\text{TiO}_2$  on FTO and  $\text{Cd}_2\text{SnO}_4$  substrates and the dark current density–voltage characteristics of the TCO/ $\text{TiO}_2$ /spiro-OMeTAD/Au devices. Their interface quality plays a key role in the performance of devices. As can be seen in

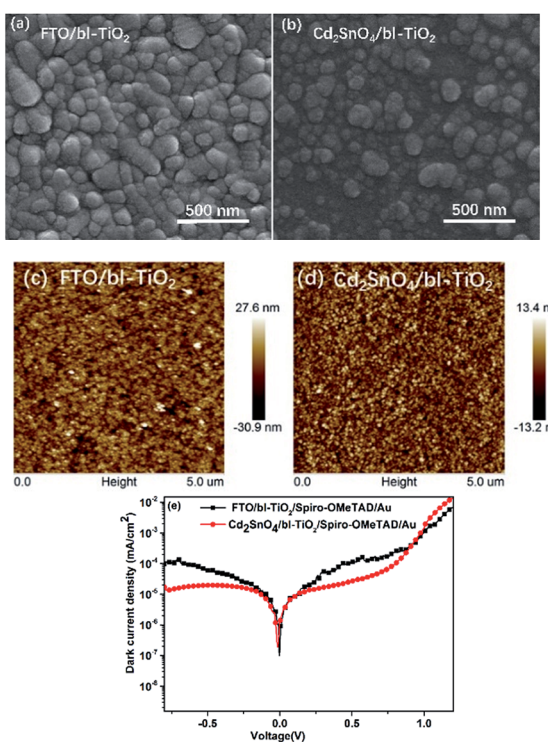


Fig. 4 SEM and AFM images of bl- $\text{TiO}_2$  on FTO (a and c) and  $\text{Cd}_2\text{SnO}_4$  (b and d) substrates; (e) dark current density–voltage characteristics of the FTO and  $\text{Cd}_2\text{SnO}_4/\text{TiO}_2/\text{spiro-OMeTAD}/\text{Au}$  devices.

Fig. 4(a–d), the morphology of  $\text{TiO}_2$  is strongly dependent on the substrate.  $\text{TiO}_2$  on the FTO substrate shows a large size compared to that on the  $\text{Cd}_2\text{SnO}_4$  substrate. Highly dense and homogeneous  $\text{TiO}_2$  films were formed by spray pyrolysis. AFM was carried out to study the morphology of different substrates. The AFM images of FTO and  $\text{Cd}_2\text{SnO}_4$  substrates are shown in ESI Fig. S1.† According to the AFM images, the surface root-mean-square (RMS) roughness of FTO,  $\text{Cd}_2\text{SnO}_4$ , FTO/ $\text{TiO}_2$ , and  $\text{Cd}_2\text{SnO}_4/\text{TiO}_2$  were 12.2 nm, 7.24 nm, 8.16 nm, and 3.97 nm, respectively. The  $\text{Cd}_2\text{SnO}_4$  and  $\text{Cd}_2\text{SnO}_4/\text{TiO}_2$  layers show lower surface roughness as compared to the FTO substrate. Note that a smooth and compact  $\text{TiO}_2$  coating layer can effectively be formed on the  $\text{Cd}_2\text{SnO}_4$  substrate due to the smaller grain size of  $\text{Cd}_2\text{SnO}_4$ . As can be observed from the dark current density–voltage curves of TCO/ $\text{TiO}_2$ /spiro-OMeTAD/Au devices, the  $\text{Cd}_2\text{SnO}_4$ -based device shows a dark current density of  $10^{-5} \text{ mA cm}^{-2}$ , which is lower than that of the FTO-based device. This indicates that charge recombination can be decreased at the electron-transporting layer/ $\text{Cd}_2\text{SnO}_4$  electrode interface. The higher surface roughness increases the interfacial charge recombination and reduces electron collection from the  $\text{TiO}_2$  layer to the electrode.<sup>17</sup>

Fig. 5(a and b) shows the typical structure configuration of perovskite device and the energy level alignment of the perovskite device employing the  $\text{Cd}_2\text{SnO}_4$ -based substrate. The glass/TCO/ $\text{TiO}_2/\text{CH}_3\text{NH}_3\text{PbI}_{3-x}\text{Cl}_x/\text{spiro-MeOTAD}/\text{Au}$  devices were fabricated. The detailed preparation approaches are discussed in the methods section. The perovskite films absorb the incident photons under light irradiation, resulting in rapid generation, drift, and diffusion of excitons in the built-in electric field. Then, photoexcited charge transfer occurs at the  $\text{TiO}_2/\text{perovskite}/\text{HTM}$  interface.<sup>36</sup> The holes of the valence band maximum position are extracted from the HOMO level of HTM. The electrons are

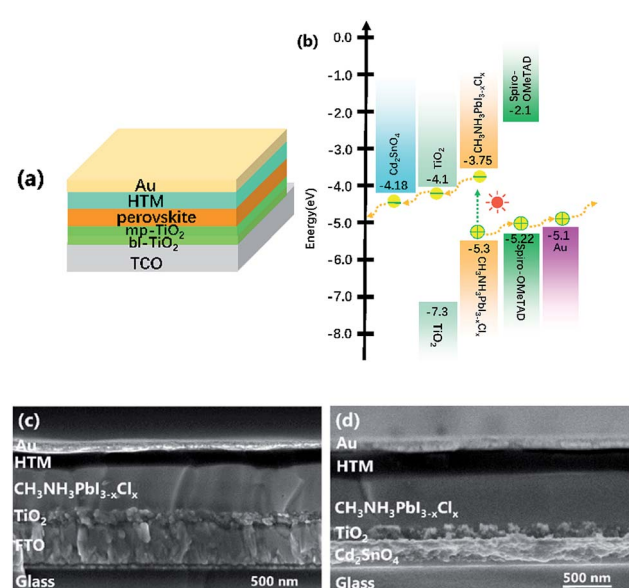


Fig. 5 (a) Structure of perovskite devices and (b) energy band diagram of the perovskite devices. Cross-sectional SEM image of the devices: (c) glass/FTO/ $\text{TiO}_2/\text{CH}_3\text{NH}_3\text{PbI}_{3-x}\text{Cl}_x/\text{spiro-MeOTAD}/\text{Au}$  and (d) glass/ $\text{Cd}_2\text{SnO}_4/\text{TiO}_2/\text{CH}_3\text{NH}_3\text{PbI}_{3-x}\text{Cl}_x/\text{spiro-MeOTAD}/\text{Au}$ .



injected into the conduction band minimum position of the  $\text{TiO}_2$  layer. Thus, the electrons are collected by the  $\text{Cd}_2\text{SnO}_4$  electrode. The matching energy-band alignment can ensure smooth carrier transport between the  $\text{TiO}_2$  and  $\text{Cd}_2\text{SnO}_4$  electrode layers.

Fig. 5(c and d) shows cross-sectional SEM images of the FTO and  $\text{Cd}_2\text{SnO}_4$ -based devices. As can be seen in the two devices, the interfacial layers are effectively contacted to ensure charge transfer. These homogeneous and dense perovskite films fabricated using a high precursor concentration method were formed on the mp- $\text{TiO}_2$  layer. The morphology of the perovskite film has been reported in a previous study.<sup>37</sup> Compared to the cross-sectional SEM images of the two devices, the thickness of FTO substrate can be up to  $\sim 400$  nm. As abovementioned, both substrates have a similar sheet resistivity of  $10\ \Omega$  per square. The thickness of  $\text{Cd}_2\text{SnO}_4$  substrate is only about 250 nm. This is important for regulating the film thickness of the front electrode, which presumably has an influence on the optical properties of the perovskite solar cells. A thicker transparent conductive oxide film decreases the optical transmittance and further affects the photovoltaic performance.

Fig. 6(a) shows the  $J$ - $V$  curves of the FTO and  $\text{Cd}_2\text{SnO}_4$ -based devices obtained under an air mass 1.5 global irradiation of  $100\ \text{mW cm}^{-2}$  for reverse and forward scanning. Table 2 lists the average photovoltaic parameters for the FTO and  $\text{Cd}_2\text{SnO}_4$ -based perovskite devices. Histograms of their device efficiency are shown in ESI Fig. S2.<sup>†</sup> Typically, the devices were investigated with a delay time of 10 ms from  $-0.1\ \text{V}$  to  $1.1\ \text{V}$  for the reverse and forward scanning direction. Both the FTO and  $\text{Cd}_2\text{SnO}_4$ -based devices exhibit slight hysteresis, as shown in Fig. 6(a), which is similar to the behavior of perovskite solar cells with a  $\text{TiO}_2$  architecture reported in other studies possibly due to the unusual defect physics and grain boundary ion migration.<sup>38–40</sup> The average photovoltaic performance parameters for the FTO-based device exhibit a PCE of 14.05%, open circuit voltage ( $V_{\text{oc}}$ ) of  $0.97\ \text{V}$ , short-circuit current density ( $J_{\text{sc}}$ ) of  $20.04\ \text{mA cm}^{-2}$ , and fill factor (FF) of 72.65% for the reverse scanning direction, and a  $J_{\text{sc}}$  of  $19.14\ \text{mA cm}^{-2}$ ,  $V_{\text{oc}}$  of  $0.90\ \text{V}$ , FF of 70.2%, and PCE of 12.1% for the forward scanning direction. For the  $\text{Cd}_2\text{SnO}_4$ -based device, the performance shows a PCE of 15.58%,  $V_{\text{oc}}$  of  $0.99\ \text{V}$ ,  $J_{\text{sc}}$  of  $21.24\ \text{mA cm}^{-2}$ , and FF of 73.83% for the reverse scanning direction, and a PCE of 14.06%,  $V_{\text{oc}}$  of  $0.94\ \text{V}$ ,  $J_{\text{sc}}$  of  $20.79\ \text{mA cm}^{-2}$ , and FF of 72.2% for the forward scanning direction. As shown in Table 2, the  $J_{\text{sc}}$ ,  $V_{\text{oc}}$ , and FF for the  $\text{Cd}_2\text{SnO}_4$ -based device are higher than those for the FTO-

Table 2 Average photovoltaic parameters of the FTO and  $\text{Cd}_2\text{SnO}_4$ -based perovskite devices. (Based on 15 devices of each group)

Substrate	$J_{\text{sc}}$ ( $\text{mA cm}^{-2}$ )	$V_{\text{oc}}$ (V)	FF (%)	PCE (%)
FTO	$20.04 \pm 1.39$	$0.97 \pm 0.03$	$72.65 \pm 2.12$	$14.05 \pm 1.3$
$\text{Cd}_2\text{SnO}_4$	$21.24 \pm 1.96$	$0.99 \pm 0.04$	$73.83 \pm 1.14$	$15.58 \pm 3.25$

based device. Specifically, a higher photocurrent can be expected from the more incident photons absorbed by the perovskite film. Due to the high transmittance in the visible spectra region of the transparent conductive oxide layer, as shown in Fig. 1, more incident photons reach the perovskite layer from the front contact. More absorption and transition from the valence band to the conduction band occur in the photoactive layer. In addition, due to the high roughness of the FTO/ $\text{TiO}_2$  interface, trapping states distributed in the energy band gap increase at the heterojunction interface, leading to an energy level offset that is deviated from the predicted level position.<sup>41</sup> In this case, electron–hole recombination loss may occur due to the undesirable charge separation efficiency in the device, contributing to the lower  $V_{\text{oc}}$  and FF.<sup>17</sup> Fig. 6(b) shows the external quantum efficiency of the devices. The spectral response of the  $\text{Cd}_2\text{SnO}_4$ -based devices begins at  $\sim 320\ \text{nm}$ , which exhibits narrow response compared to that of the FTO-based devices due to the lower optical energy band gap. This is consistent with the transmittance spectra, as shown in Fig. 1(a). The EQE dramatically increases in the  $500\text{--}600\ \text{nm}$  spectral range. This suggests that efficient charge extraction and transportation occur in the built-in electric field for the  $\text{Cd}_2\text{SnO}_4$ -based device, leading to a higher photogenerated current.

We further analyzed the  $I$ - $V$  properties of the solar cells. According to the Shockley equation and equivalent circuit model for a single heterojunction solar cell, the  $I$ - $V$  characteristic equation is described as follows:<sup>42,43</sup>

$$J = -J_{\text{sc}} + J_0 \left\{ \exp \left[ \frac{e(V - JR_s)}{nkT} \right] - 1 \right\} + \frac{V - JR_s}{R_{\text{sh}}} \quad (4)$$

where,  $J$ ,  $J_{\text{sc}}$ ,  $J_0$ ,  $e$ ,  $V$ ,  $n$ ,  $k$ ,  $R_s$ ,  $R_{\text{sh}}$ , and  $T$  represent current density, short-circuit current density, recombination current density, electric charge, bias voltage, diode ideality factor, Boltzmann constant, series resistance, shunt resistance, and temperature, respectively. Based on the differential equation and mathematical conversion, eqn (4) can be written as

$$\frac{dV}{dJ} = \frac{nkT}{e} \left( \frac{1 - R_{\text{sh}}^{-1} \frac{dV}{dJ}}{J + J_{\text{sc}} - V/R_{\text{sh}}} \right) + R_s \quad (5)$$

$$\ln(J + J_{\text{sc}} - V/R_{\text{sh}}) = \frac{e}{nkT} (V - R_s J) + \ln J_0 \quad (6)$$

For perovskite devices, the shunt resistances of the devices are estimated to be  $3000\ \Omega\ \text{cm}^2$ .<sup>42</sup> The value of  $R_s$  is the intercept by linear curve fitting, as shown in Fig. 7(a). The series resistance of FTO and  $\text{Cd}_2\text{SnO}_4$ -based devices was estimated to be  $1.63\ \Omega\ \text{cm}^2$  and  $1.46\ \Omega\ \text{cm}^2$ , respectively. This indicates that the  $\text{Cd}_2\text{SnO}_4$ -

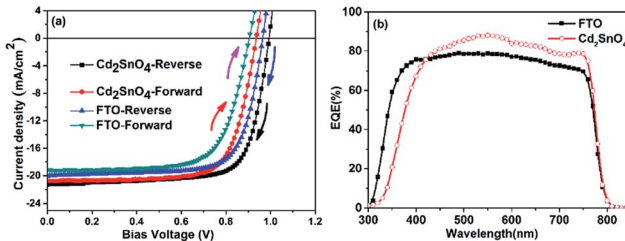


Fig. 6 (a) Typical  $J$ - $V$  curve of the FTO and  $\text{Cd}_2\text{SnO}_4$ -based devices obtained under AM1.5 light irradiation for the reverse and forward scanning directions and (b) EQE spectra of the devices.



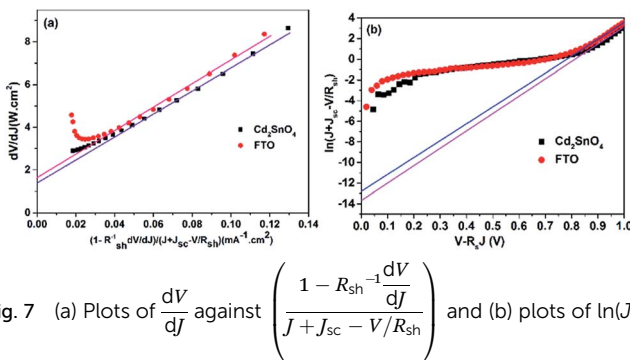


Fig. 7 (a) Plots of  $\frac{dV}{dJ}$  against  $\left( \frac{1 - R_{sh}^{-1} \frac{dV}{dJ}}{J + J_{sc} - V/R_{sh}} \right)$  and (b) plots of  $\ln(J + J_{sc} - V/R_{sh})$  against  $(V - R_{sh} J)$ .

based device shows a lower series resistance due to the thickness of the films. Similarly, the value of  $J_0$  can be obtained by linear curve fitting, as shown in Fig. 7(b). The values of the intercept for the FTO and Cd<sub>2</sub>SnO<sub>4</sub>-based devices are -12.85 and -13.67 and the recombination current density can be estimated to be  $2.62 \times 10^{-6}$  mA cm<sup>-2</sup> and  $1.16 \times 10^{-6}$  mA cm<sup>-2</sup>, respectively. The lower  $J_0$  of the Cd<sub>2</sub>SnO<sub>4</sub>-based devices indicates that interface charge recombination loss can be effectively decreased by interfacial engineering, leading to a higher  $V_{oc}$  and FF.

The steady-state photoluminescence and time-resolved photoluminescence spectra were acquired to explore the photoinduced charge dynamical process in the devices. We prepared CH<sub>3</sub>NH<sub>3</sub>PbI<sub>3-x</sub>Cl<sub>x</sub> films on FTO/TiO<sub>2</sub> and Cd<sub>2</sub>SnO<sub>4</sub>/TiO<sub>2</sub> substrates. Fig. 8(a) presents the steady-state photoluminescence spectra for CH<sub>3</sub>NH<sub>3</sub>PbI<sub>3-x</sub>Cl<sub>x</sub> films on FTO/TiO<sub>2</sub> and Cd<sub>2</sub>SnO<sub>4</sub>/TiO<sub>2</sub> substrates. The PL intensity at 773 nm for the perovskite film on Cd<sub>2</sub>SnO<sub>4</sub>/TiO<sub>2</sub> clearly shows a decrease as compared to that for the perovskite film on the FTO/TiO<sub>2</sub> substrate. This indicates that the charge dissociation process on the Cd<sub>2</sub>SnO<sub>4</sub> electrode with TiO<sub>2</sub> layer is more efficient. Fig. 8(b) shows the time-resolved photoluminescence spectra of the perovskite films on various substrates. The PL decay lifetimes were obtained by fitting the data to the biexponential decay function containing a fast decay component ( $\tau_1$ ) and a slow decay component ( $\tau_2$ ). The detailed fitting parameters are summarized in ESI Table S2.† The fast decay component might be considered as the result of the quenching of free electrons in the perovskite *via* transport to TiO<sub>2</sub>. The slow decay component can be originated from the radiative recombination of the free carriers in the perovskite film.<sup>15,44,45</sup> For the FTO/TiO<sub>2</sub>/CH<sub>3</sub>NH<sub>3</sub>PbI<sub>3-x</sub>Cl<sub>x</sub> film sample, the fast decay

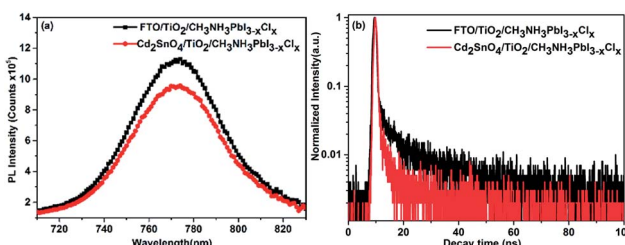


Fig. 8 (a) Steady-state photoluminescence spectra and (b) time-resolved photoluminescence spectra of the CH<sub>3</sub>NH<sub>3</sub>PbI<sub>3-x</sub>Cl<sub>x</sub> films on the FTO/TiO<sub>2</sub> and Cd<sub>2</sub>SnO<sub>4</sub>/TiO<sub>2</sub> substrates.

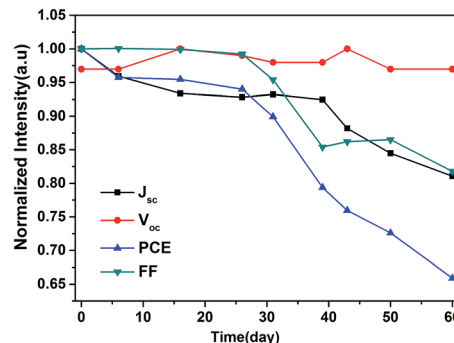


Fig. 9 Stability of the device stored in a relative humidity of  $\sim 10\%$  for 60 days.

lifetime was 0.55 ns and the slow decay lifetime was 14.4 ns, whereas the weight fractions were 67.7% and 32.3%, respectively. This indicates that the decay of free charges was dominated by charge collection through the TiO<sub>2</sub>/perovskite interface. However, the  $\tau_1$  and  $\tau_2$  for the Cd<sub>2</sub>SnO<sub>4</sub>/TiO<sub>2</sub>/CH<sub>3</sub>NH<sub>3</sub>PbI<sub>3-x</sub>Cl<sub>x</sub> sample decreased to 0.46 ns and 9.26 ns, respectively. The weight fraction of the fast decay component drastically increased to 89.6%. The Cd<sub>2</sub>SnO<sub>4</sub> electrode facilitates faster charge transfer from perovskite to TiO<sub>2</sub>. The electrode can enable the much faster and more efficient collection of the photogenerated electrons due to lower interfacial recombination loss as discussed above, leading to the enhancement of photovoltaic performance.<sup>15</sup>

Furthermore, we investigated the long-term device stability of the Cd<sub>2</sub>SnO<sub>4</sub>-based device in a relative humidity of  $\sim 10\%$  at room temperature, as shown in Fig. 9. The stability of the FTO-based device is shown in ESI Fig. S3.†

When the device was stored for 60 days, the  $V_{oc}$  showed a slight decay. The device efficiency drops  $\sim 35\%$  after 60 days. The FF and  $J_{sc}$  of the device maintained 85% of its initial value. For the FTO-based device, the FF and  $J_{sc}$  of the device can retain  $\sim 95\%$  of the initial value when the device was stored for 25 days. The dense HTM layer hinders the penetration of water molecule for a long time, which can improve the device stability. The device parameters did not show significant degradation in two months. However, the instability of perovskite devices is the main issue while exposing them to an ambient air environment. Moisture degradation and photooxidation may take place at the interface in the presence of oxygen, light, and moisture. Further enhancements of the stability of the device are required. Interface modification on TiO<sub>2</sub>/CH<sub>3</sub>NH<sub>3</sub>PbI<sub>3-x</sub>Cl<sub>x</sub> may be an effective method to improve the stability. In further studies, we believe that the introduction of surface treatment technology by passivation surface defects of TiO<sub>2</sub> layer to protect the perovskite devices from corrosion by moisture and oxygen is required. Solving the extrinsic and intrinsic degradation problem of the perovskite devices, which have potential for large scale applications, overcomes the major obstacles in their practical applications.

## Conclusion

We demonstrated a new structure of perovskite solar cell using a Cd<sub>2</sub>SnO<sub>4</sub> transparent conducting oxide substrate. Owing to

its higher electrical conductivity, optical transmission in the visible range, and lower surface roughness as compared to those of FTO, a higher PCE of 15.58% for the  $\text{Cd}_2\text{SnO}_4$ -based perovskite solar cell was obtained. The energy band structure and interfacial characteristics of  $\text{Cd}_2\text{SnO}_4/\text{TiO}_2$  interface were investigated. The results showed that the matching energy band alignment could ensure smooth carrier transport and collection between the  $\text{TiO}_2$  and  $\text{Cd}_2\text{SnO}_4$  electrode layers, which suggests that  $\text{Cd}_2\text{SnO}_4$  transparent conducting oxide would be the most promising candidate for high performance perovskite solar cells.

## Acknowledgements

This work was financially supported by the Science and Technology Program of Sichuan Province (No. 2016GZX0272) and the Innovation Program of Sichuan University (No. 201510611374, No. 201510610799 and No. 201510610437).

## References

- 1 D. P. McMeekin, G. Sadoughi, W. Rehman, G. E. Eperon, M. Saliba, M. T. Horantner, A. Haghhighirad, N. Sakai, L. Korte, B. Rech, M. B. Johnston, L. M. Herz and H. J. Snaith, *Science*, 2016, **351**, 151–155.
- 2 D. Bi, W. Tress, M. I. Dar, P. Gao, J. Luo, C. Renevier, K. Schenk, A. Abate, F. Giordano, J. P. Correa Baena, J. D. Decoppet, S. M. Zakeeruddin, M. K. Nazeeruddin, M. Gratzel and A. Hagfeldt, *Sci. Adv.*, 2016, **2**, e1501170.
- 3 D. Liu, L. Wu, C. Li, S. Ren, J. Zhang, W. Li and L. Feng, *ACS Appl. Mater. Interfaces*, 2015, **7**, 16330–16337.
- 4 Q. Tai, P. You, H. Sang, Z. Liu, C. Hu, H. L. W. Chan and F. Yan, *Nat. Commun.*, 2016, **7**, 11105.
- 5 X. Li, D. Bi, C. Yi, J.-D. Décoppet, J. Luo, S. M. Zakeeruddin, A. Hagfeldt and M. Grätzel, *Science*, 2016, **353**, 58–62.
- 6 Z. Zhou, J. Xu, L. Xiao, J. Chen, Z. A. Tan, J. Yao and S. Dai, *RSC Adv.*, 2016, **6**, 78585–78594.
- 7 L. F. Zhu, Y. Z. Xu, J. J. Shi, H. Y. Zhang, X. Xu, Y. H. Zhao, Y. H. Luo, Q. B. Meng and D. M. Li, *RSC Adv.*, 2016, **6**, 82282–82288.
- 8 Z. Zhang, X. Yue, D. Wei, M. Li, P. Fu, B. Xie, D. Song and Y. Li, *RSC Adv.*, 2015, **5**, 104606–104611.
- 9 D. Liu, C. Liu, L. Wu, W. Li, F. Chen, B. Xiao, J. Zhang and L. Feng, *RSC Adv.*, 2016, **6**, 51279–51285.
- 10 X. Xia, W. Wu, H. Li, B. Zheng, Y. Xue, J. Xu, D. Zhang, C. Gao and X. Liu, *RSC Adv.*, 2016, **6**, 14792–14798.
- 11 H. Sohrabpoor, G. Puccetti and N. E. Gorji, *RSC Adv.*, 2016, **6**, 49328–49334.
- 12 W.-C. Lai, K.-W. Lin, Y.-T. Wang, T.-Y. Chiang, P. Chen and T.-F. Guo, *Adv. Mater.*, 2016, **28**, 3290–3297.
- 13 H. Hwang, A. Kim, Z. Zhong, H.-C. Kwon, S. Jeong and J. Moon, *Adv. Funct. Mater.*, 2016, **26**, 6545–6554.
- 14 M. Dianetti, F. Di Giacomo, G. Polino, C. Ciceroni, A. Liscio, A. D'Epifanio, S. Licoccia, T. M. Brown, A. Di Carlo and F. Brunetti, *Sol. Energy Mater. Sol. Cells*, 2015, **140**, 150–157.
- 15 Y. Li, L. Meng, Y. M. Yang, G. Xu, Z. Hong, Q. Chen, J. You, G. Li, Y. Yang and Y. Li, *Nat. Commun.*, 2016, **7**, 10214.
- 16 K. Sun, P. C. Li, Y. J. Xia, J. J. Chang and J. Y. Ouyang, *ACS Appl. Mater. Interfaces*, 2015, **7**, 15314–15320.
- 17 H. Sung, N. Ahn, M. S. Jang, J.-K. Lee, H. Yoon, N.-G. Park and M. Choi, *Adv. Energy Mater.*, 2016, **6**, 1501873.
- 18 J. A. Stoke, J. D. Beach, W. C. Bradford and T. R. Ohno, *Thin Solid Films*, 2014, **562**, 254–259.
- 19 X. Wu, *Sol. Energy*, 2004, **77**, 803–814.
- 20 B. A. Korevaar, J. R. Cournoyer, O. Sulima, A. Yakimov and J. N. Johnson, *Prog. Photovoltaics Res. Appl.*, 2014, **22**, 1040–1049.
- 21 S. M. Al-Sofiani and H. E. Hassan, *J. Alloys Compd.*, 2015, **651**, 149–156.
- 22 R. Kumaravel and K. Ramamurthi, *J. Alloys Compd.*, 2011, **509**, 4390–4393.
- 23 R. Mamazza, D. L. Morel and C. S. Ferekides, *Thin Solid Films*, 2005, **484**, 26–33.
- 24 G. Valincius, V. Reipa, V. Vilker, J. T. Woodward and M. Vaudin, *J. Electrochem. Soc.*, 2001, **148**, E341–E347.
- 25 R. B. H. Tahar, T. Ban, Y. Ohya and Y. Takahashi, *J. Am. Ceram. Soc.*, 2001, **84**, 85–91.
- 26 J. H. Im, I. H. Jang, N. Pellet, M. Gratzel and N. G. Park, *Nat. Nanotechnol.*, 2014, **9**, 927–932.
- 27 J. Tauc, *Mater. Res. Bull.*, 1968, **3**, 37–46.
- 28 M. A. Green, A. Ho-Baillie and H. J. Snaith, *Nat. Photonics*, 2014, **8**, 506–514.
- 29 J. Werner, C.-H. Weng, A. Walter, L. Fesquet, J. P. Seif, S. De Wolf, B. Niesen and C. Ballif, *J. Phys. Chem. Lett.*, 2016, **7**, 161–166.
- 30 T. Duong, N. Lal, D. Grant, D. Jacobs, P. Zheng, S. Rahman, H. Shen, M. Stocks, A. Blakers, K. Weber, T. P. White and K. R. Catchpole, *IEEE J. Photovolt.*, 2016, **6**, 679–687.
- 31 J. Werner, G. Dubuis, A. Walter, P. Löper, S.-J. Moon, S. Nicolay, M. Morales-Masis, S. De Wolf, B. Niesen and C. Ballif, *Sol. Energy Mater. Sol. Cells*, 2015, **141**, 407–413.
- 32 Y. Park, V. Choong, Y. Gao, B. R. Hsieh and C. W. Tang, *Appl. Phys. Lett.*, 1996, **68**, 2699–2701.
- 33 A. Dymshits, A. Henning, G. Segev, Y. Rosenwaks and L. Etgar, *Sci. Rep.*, 2015, **5**, 8704.
- 34 J. Shi, X. Xu, D. Li and Q. Meng, *Small*, 2015, **11**, 2472–2486.
- 35 Z. Zhou, S. Pang, Z. Liu, H. Xu and G. Cui, *J. Mater. Chem. A*, 2015, **3**, 19205–19217.
- 36 G. Xing, B. Wu, S. Chen, J. Chua, N. Yantara, S. Mhaisalkar, N. Mathews and T. C. Sum, *Small*, 2015, **11**, 3606–3613.
- 37 D. Liu, C. Liu, L. Wu, W. Li, F. Chen, B. Xiao, J. Zhang and L. Feng, *RSC Adv.*, 2016, **6**, 51279–51285.
- 38 S. Wozny, M. Yang, A. M. Nardes, C. C. Mercado, S. Ferrere, M. O. Reese, W. Zhou and K. Zhu, *Chem. Mater.*, 2015, **27**, 4814–4820.
- 39 H.-S. Kim and N.-G. Park, *J. Phys. Chem. C*, 2014, **5**, 2927–2934.
- 40 Y. Shao, Y. Fang, T. Li, Q. Wang, Q. Dong, Y. Deng, Y. Yuan, H. Wei, M. Wang, A. Gruverman, J. Shield and J. Huang, *Energy Environ. Sci.*, 2016, **9**, 1752–1759.
- 41 Q.-K. Wang, R.-B. Wang, P.-F. Shen, C. Li, Y.-Q. Li, L.-J. Liu, S. Duham and J.-X. Tang, *Adv. Mater. Interfaces*, 2015, **2**, 1400528.
- 42 J. Shi, J. Dong, S. Lv, Y. Xu, L. Zhu, J. Xiao, X. Xu, H. Wu, D. Li, Y. Luo and Q. Meng, *Appl. Phys. Lett.*, 2014, **104**, 063901.



- 43 J. Qing, H.-T. Chandran, Y.-H. Cheng, X.-K. Liu, H.-W. Li, S.-W. Tsang, M.-F. Lo and C.-S. Lee, *ACS Appl. Mater. Interfaces*, 2015, **7**, 23110–23116.
- 44 P.-W. Liang, C.-Y. Liao, C.-C. Chueh, F. Zuo, S. T. Williams, X.-K. Xin, J. Lin and A. K. Y. Jen, *Adv. Mater.*, 2014, **26**, 3748–3754.
- 45 Y. Shi, Y. Xing, Y. Li, Q. Dong, K. Wang, Y. Du, X. Bai, S. Wang, Z. Chen and T. Ma, *J. Phys. Chem. C*, 2015, **119**, 15868–15873.

